

# Simulations of light scattering from a biconcave red blood cell using the finite-difference time-domain method

**Jun Q. Lu**

East Carolina University  
Department of Physics  
Greenville, North Carolina  
E-mail: [luj@mail.ecu.edu](mailto:luj@mail.ecu.edu)

**Ping Yang**

Texas A & M University  
Department of Atmospheric Sciences  
College Station, Texas

**Xin-Hua Hu**

East Carolina University  
Department of Physics  
Greenville, North Carolina

**Abstract.** Numerical simulations of light scattering by a biconcave shaped human red blood cell (RBC) are carried out using the finite-difference time-domain (FDTD) method. A previously developed FDTD code for the study of light scattering by ice crystals is modified for the current purpose and it is validated against Mie theory using a spherically shaped RBC. Numerical results for the angular distributions of the Mueller scattering matrix elements of an RBC and their dependence on shape, orientation, and wavelength are presented. Also calculated are the scattering and absorption efficiencies. The implication of these results on the possibility of probing RBC shape changes is discussed. © 2005 Society of Photo-Optical Instrumentation Engineers.

[DOI: 10.1117/1.1897397]

Keywords: red blood cell; cell scattering; finite-difference time-domain method; Mueller scattering matrix.

Paper 04019 received Feb. 17, 2004; revised manuscript received Jun. 25, 2004; accepted for publication Aug. 27, 2004; published online Apr. 4, 2005.

## 1 Introduction

A hospital laboratory on average examines about 300 blood samples *in vitro* for diagnostic purposes daily.<sup>1</sup> As a prominent component of blood, mature human red blood cells (RBCs) are light scatterers with homogeneous bodies enclosed by membranes and have attracted significant attention for optical diagnosis of disorders related to RBCs and blood. Flow cytometry is an established technique for automatic measurement and/or sorting of RBCs through detection of scattered light featured with good SNRs and detection simplicity and no necessity for cell staining.<sup>1</sup> In ektacytometry it has been demonstrated experimentally<sup>2,3</sup> that the distribution of the forward light scattering depends on the size, shape, and composition of individual RBCs. To better understand existing experimental data, develop new optical diagnostic tools, and provide important information for understanding light-tissue interaction *in vivo* and *in vitro*, it is essential to quantitatively model light scattering by a single RBC.

RBCs possess intriguing biconcave shapes, which vary with the pressure and physiological and pathological conditions found in blood flow. For example, it has been reported that the biconcave shape can change toward a cup (stomatocytic) shape or a spiculated (echinocytic) shape as a result of variation in the ionic strength and pH values of the immersion medium.<sup>4</sup> The size parameters of RBCs are in the range of 10 to 50 for wavelengths of general interest, where the size parameter ( $\alpha$ ) is defined as  $(2\pi R)/\lambda$  with  $2R$  as the characteristic size of the particle and  $\lambda$  as the light wavelength in the surrounding medium. No analytical solutions can be found for light scattering from scatterers with these properties. Early

investigations of light scattering by RBCs have used Mie theory, with the sphere as either an approximate model<sup>5</sup> or an accurate model of spherical RBC obtained through chemical treatment.<sup>6</sup> In ektacytometry based studies, light scattering by RBCs has been investigated with an anomalous diffraction approximation by assuming ellipsoidal shapes.<sup>7</sup> Light scattering by an RBC of undeformed biconcave shape has been analyzed using a straight-ray approximation.<sup>8</sup> This approximation is valid only in the small scattering angle region under the condition of small refractive index of RBC relative to the surrounding medium. Recently, a boundary-element method was developed to solve the scattering problem of axisymmetry for an undeformed RBC of biconcave shape aligned with the direction of incident light.<sup>9,10</sup> The boundary-element method has the advantages of high accuracy and low computational cost for scatterers of axisymmetric shapes and homogeneous bodies. But these advantages no longer hold when it comes to general cases of light scattering from biological cells, where arbitrary shape and inhomogeneous dielectric response within the cell are common.

Cellular scattering of light at large angles toward the backscattering direction was demonstrated experimentally to contain rich information on cellular structure.<sup>11</sup> Therefore, it is highly desirable to develop reliable methods to model light scattering by individual RBCs with an arbitrary shape in the full range of scattering angles. In general, numerical methods must be used to model light scattering processes by biological cells with complex shapes and inhomogeneous bodies. Recently, Mishchenko et al.<sup>12</sup> comprehensively reviewed the light scattering computational methods, which include the T-matrix method,<sup>13</sup> the discrete dipole approximation,<sup>14,15</sup> and

Address all correspondence to Professor Jun Q. Lu, East Carolina University, Department of Physics, Greenville, NC 27858

the finite-difference time-domain (FDTD) technique.<sup>16–20</sup> In this paper, we use the FDTD method to compute the scattering properties of a single RBC. Although computationally intensive for three-dimensional (3-D) problems, this method employs an algorithm that is simple to adapt to a wide variety of biological cells for calculating scattered electromagnetic fields. Furthermore, the computational time of the FDTD calculations can be significantly reduced using parallel computing techniques; making it attractive as the computing power and storage size increase rapidly at a constant cost. The FDTD method has been applied to light scattering from epithelial cells to investigate the effect of intracellular components<sup>21,22</sup> and to study the effects of shape change in RBCs,<sup>23</sup> and the results of these studies demonstrate the potential of the application of the FDTD method in cell scattering studies. As a prelude to our long-term effort in accurate modeling of light scattering from biological cells,<sup>24</sup> we investigated numerically the light scattering properties of a biconcave RBC with a serial FDTD code. In this paper, we present results on Mueller scattering matrix calculations of scattered light by an RBC of biconcave shape and their dependence on wavelength of light and the shape and orientation of the cell. The FDTD method and modeling of RBC are described in the next section, followed by results and discussions.

## 2 Mathematical Modeling

### 2.1 Scattering Theory

We developed a serial FDTD code for the study of light scattering by an RBC based on a code previously designed for ice crystal scattering,<sup>17,25</sup> and a brief review of the method is given here. In solving the problem of light scattering by a biological cell, we consider a wave incident on the cell in an open space filled with a homogeneous and nonferromagnetic medium. The medium is characterized by a permittivity constant  $\epsilon_0$ , while the cellular structure by a dielectric function  $\epsilon(\mathbf{r})$ . The electromagnetic fields in the system satisfy the Maxwell equations and the general solution of the electromagnetic fields in the frequency domain is obtained by applying the Green's second identity to the wave equations in the region. At distances far from the scatterer, the scattered field takes the following form:<sup>26</sup>

$$\mathbf{E}_s(\mathbf{r}, \omega) = \mathbf{F}(\mathbf{k}, \mathbf{k}_0) \frac{e^{ikr}}{r}, \quad (1)$$

where  $\mathbf{k}$  and  $\mathbf{k}_0$  are the wave vectors of the scattering and incident fields, respectively, and the amplitude function  $\mathbf{F}(\mathbf{k}, \mathbf{k}_0)$  is given by

$$\begin{aligned} \mathbf{F}(\mathbf{k}, \mathbf{k}_0) &= \frac{1}{4\pi} \int_V (k^2 + \nabla \nabla \cdot) \left[ \frac{\epsilon(\mathbf{r}', \omega)}{\epsilon_0} - 1 \right] \mathbf{E}(\mathbf{r}', \omega) \\ &\quad \times \exp(-i\mathbf{k} \cdot \mathbf{r}') d^3r', \end{aligned} \quad (2)$$

where  $V$  indicates the cell volume. When polarization is taken into consideration, Eq. (1) can be written in the following matrix form:<sup>27</sup>

$$\begin{pmatrix} E_{\parallel s} \\ E_{\perp s} \end{pmatrix} = \frac{\exp(-ikr)}{-ikr} \begin{pmatrix} S_2 S_3 \\ S_4 S_1 \end{pmatrix} \begin{pmatrix} E_{\parallel i} \\ E_{\perp i} \end{pmatrix} \quad (3)$$

by resolving the incident and scattering fields into components parallel and perpendicular to the scattering plane. The elements of the  $2 \times 2$  amplitude matrix in Eq. (3) are complex functions of the angle between  $\mathbf{k}$  and  $\mathbf{k}_0$ , which is described by the scattering angle  $\theta_s$  and the azimuthal angle  $\phi_s$  of the scattering plane, and they can be calculated from  $\mathbf{F}(\mathbf{k}, \mathbf{k}_0)$  using two incident waves of independent polarization.<sup>17</sup> To obtain the scattered field  $\mathbf{E}_s(\mathbf{r}, \omega)$ , the integral in Eq. (2) must be evaluated first, which requires the knowledge of the near field  $\mathbf{E}(\mathbf{r}, \omega)$ , i.e., the field inside the cell. As discussed earlier, to obtain the near field for a scatterer with arbitrary shape and possible complex internal structure, the FDTD method can be used.

The FDTD method numerically solves the Maxwell equations in the time domain. In this method, the region that consists of the scatterer and its surrounding medium is discretized into rectangular grid cells, with the grid points denoted by the indices  $(I, J, K) = (I\Delta x, J\Delta y, K\Delta z)$ , where  $\Delta x$ ,  $\Delta y$ , and  $\Delta z$  are the dimensions of a grid cell in the  $x$ ,  $y$ , and  $z$  directions, respectively. And the time is also discretized with a step size of  $\Delta t$ , so the time at the  $n$ 'th time step is<sup>16</sup>  $t = n\Delta t$ . The shape and internal structure of the scatterer is realized numerically by assigning the values of  $\epsilon(\mathbf{r})$  over the grid. This feature enables simulations for scatterers of arbitrary shape and structure. The FDTD method in this paper uses first-order central difference approximations for the spatial and temporal derivatives in the two curl equations and solves the resultant set of explicit finite-difference equations in a time-marching sequence with time step size  $\Delta t$ . The central difference approximation and the nature of the curl equations require that the electric and magnetic fields be evaluated at staggered locations in space (the Yee cell) and the two fields be updated alternatively in time steps, this setting also implicitly enforces the divergence equations in the Maxwell equations. In addition, the unbounded simulating region must be limited to just enclose the scatterer for computational efficiency, and this is often achieved by introducing an artificial absorbing boundary condition (ABC) at the perimeter of the finite domain to minimize artificial reflections of outgoing waves. In the calculations presented, the perfectly matched layer (PML) absorbing boundary condition is used.<sup>28</sup>

Furthermore, the incident source will be considered only in the region very close to the scatterer for simplicity. This enables the separation of the computational domain into two different regions: the region close to the scatterer, where the total field (incident and scattered field) will be considered, and the outer region including the PML, where only the scattered field will be considered. In the presented calculations, the incident field is represented<sup>25</sup> by a plane wave of a Gaussian pulse over a temporal window of  $10w$  with  $E_{\text{inc}}(t) = \exp[-(t/w-5)^2]$  and the width  $w = 30\Delta t$ . Using a pulsed incident field requires that the time-marching process be long enough to ensure the energy remaining in the system be reduced to a significantly low level.<sup>17</sup> The near field solved by the FDTD method is in the time domain and must be transformed into its counterpart in the frequency domain with a discrete Fourier transform for evaluation of the scattered field in Eqs. (1) and (2). The volume integral approach<sup>17</sup> presented in Eq. (2) for obtaining the scattering waves in the far field was chosen for its efficiency and reduced errors in dealing with an absorbing scatterer over the surface integral method.<sup>16</sup>

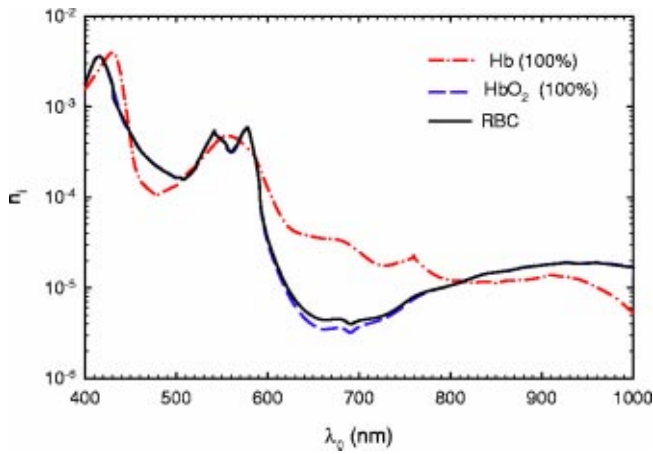


**Fig. 1** Imaginary refractive indices of Hb, HbO<sub>2</sub>, and a normal RBC as a function of wavelength  $\lambda_0$  with  $h_1=97\%$ .

Previous studies demonstrated that measurements of polarized light scattering depend sensitively on cell morphology and thus can be used to sort cells of different species and strains.<sup>29–31</sup> Therefore, complete characterization of a light scattering process requires consideration of the polarization of the incident and scattered light fields. Light of arbitrary polarization can be represented by four numbers known as the Stokes parameters ( $I, Q, U, V$ ). The Stokes parameters for the incident light and scattered light are related through the Mueller scattering matrix:<sup>27</sup>

$$\begin{pmatrix} I_s \\ Q_s \\ U_s \\ V_s \end{pmatrix} = \frac{1}{k^2 r^2} \begin{pmatrix} S_{11} & S_{12} & S_{13} & S_{14} \\ S_{21} & S_{22} & S_{23} & S_{24} \\ S_{31} & S_{32} & S_{33} & S_{34} \\ S_{41} & S_{42} & S_{43} & S_{44} \end{pmatrix} \begin{pmatrix} I_i \\ Q_i \\ U_i \\ V_i \end{pmatrix}. \quad (4)$$

The 16 elements in the Mueller scattering matrix are real functions of both wavelength ( $\lambda$ ) and scattering angles ( $\theta_s$  and  $\phi_s$ ), and they depend on the composition of the scatterer and the scattering configuration through their relations with the elements of the amplitude matrix.<sup>27,32</sup> Each element in the Mueller scattering matrix describes a different aspect of the scattering related to the morphology of the scatterer.<sup>33</sup> For example, the normalized element  $S_{11}$ , known as the phase function, yields the probability of an unpolarized incident light being scattered in a direction, and it has been reported that  $S_{34}$  is very sensitive to structural variations.<sup>29,33</sup> Complete knowledge of the scattering properties of a scatterer requires that the independent elements of the Mueller scattering matrix be known. For an undeformed RBC with a given orientation, only 6 of the 16 matrix elements are independent, which reduce to 4 for certain orientations of high symmetry or sphere cases.<sup>32</sup>

Based on the preceding discussion, we calculated the angular distribution of the Mueller scattering matrix of an RBC with different shapes, orientations, and wavelengths. In the following results, the phase function  $S_{11}$  is normalized over the range of solid scattering angle ( $\Omega_s$ ):

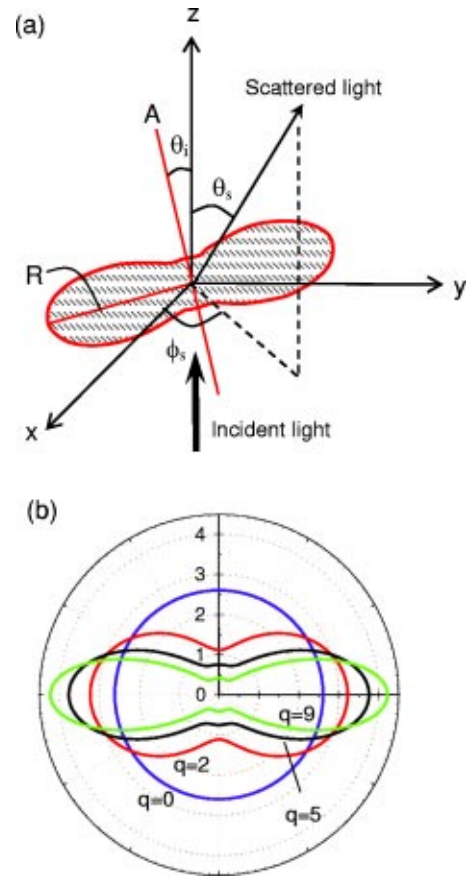


**Fig. 2** (a) Configuration of light scattering by an RBC, where the scattering plane is defined by the propagation direction of the incident light of  $z$  axis and that of the scattered light and marked by the two dashed lines; and (b) the cross sections of undeformed ( $q=5$ ) and deformed RBC of biconcave disk shapes in a polar plot.

$$\frac{1}{4\pi} \int_{4\pi} S_{11}(\theta_s, \phi_s) d\Omega_s = 1. \quad (5)$$

In addition to the scattering matrix, single scattering optical parameters, including the anisotropy factor  $g$  [ $= \int_{4\pi} S_{11}(\theta_s, \phi_s) \cos \theta_s d\Omega_s / \int_{4\pi} S_{11}(\theta_s, \phi_s) d\Omega_s$ ], are obtained to characterize the scatterer. The cross sections of scattering ( $\sigma_s$ ) and absorption ( $\sigma_a$ ) are expressed in terms of the dimensionless efficiency factors of scattering ( $Q_s$ ) and absorption ( $Q_a$ ) that are defined as the ratios of the respective cross sections to the geometrical cross section  $\sigma_g$ .

### 2.2 RBC Modeling

A mature human RBC is a nonnucleated cell filled with an aqueous solution of hemoglobin proteins within the membrane and is modeled in this report as a homogenous biconcave body. The hemoglobin proteins have different derivatives according to their binding molecules and we consider only the two major components of oxyhemoglobin (HbO<sub>2</sub>) and deoxyhemoglobin (Hb). For a homogeneous RBC, the refractive index  $n = n_r + in_i$  is treated as a constant within the cell with the imaginary part given by

$$n_i = \frac{\ln 10}{4\pi} \frac{c\lambda_0}{n_r} (h_1\gamma_1 + h_2\gamma_2), \quad (6)$$

where  $\lambda_0$  is the light wavelength in free space,  $c$  is the hemoglobin concentration, and  $h_1$  and  $h_2$  ( $=1-h_1$ ) and  $\gamma_1$  and  $\gamma_2$  are the volume ratio and molar extinction coefficients of HbO<sub>2</sub> and Hb, respectively. The spectroscopy data of  $\gamma_1$  and  $\gamma_2$  were reported for  $\lambda_0$  ranging from 200 to 1000 nm in Ref. 34. We assumed a hemoglobin oxygen saturation of  $h_1=97\%$  for a normal RBC and a constant value of  $n_r=1.400$  because the wavelength dependence of the real refractive index is not known but expected to be weak in this spectral region.<sup>7</sup> In addition, we adopted  $c=335$  g/l or  $5.04 \times 10^{-3}$  mole/liter for the hemoglobin concentration.<sup>35</sup> With these data, the imaginary refractive index of a normal RBC was calculated as a function of  $\lambda_0$  between 400 and 1000 nm and is plotted in Fig. 1. Note here that the value of  $n_i$  calculated in this paper is about one order of magnitude smaller than that reported in Ref. 8. In calculating the scattered fields, we assumed that the RBC is suspended in blood plasma which is transparent to the light wavelength considered in this study with a constant refractive index  $n_p=1.350$ .

Human RBCs possess a viscoelastic structure and can change shape isovolumetrically in response to different shear or physiologic conditions, resulting in significant pathological consequences.<sup>4,36</sup> In modeling the shape of the RBC, we employed a simple surface function introduced in Ref. 8 to describe the biconcave disc shape of the RBC as

$$r(\theta_A, \phi_A) = a \sin^q \theta_A + b, \quad (7)$$

where  $\theta_A$  and  $\phi_A$  are the polar and azimuthal angles in spherical coordinates relative to the axis of rotational symmetry,

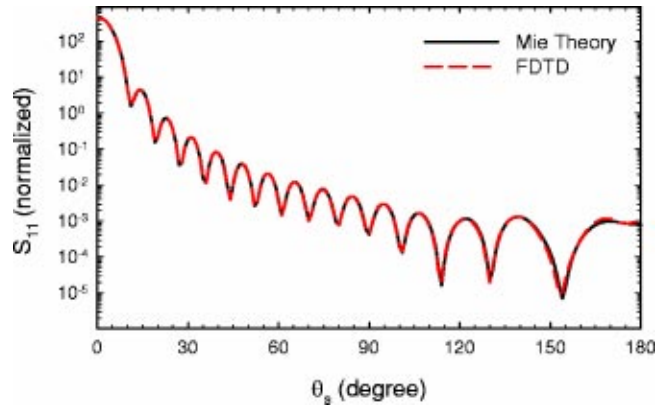


**Fig. 3** Mueller scattering matrix element  $S_{11}$  calculated by FDTD and Mie theory for a homogenous sphere with radius  $R=2.655 \mu\text{m}$ ,  $n_r/n_p=1.0385$ , and  $n_i=1.6804 \times 10^{-5}$  at wavelength  $\lambda_0=1 \mu\text{m}$ . Grid size factor for the FDTD calculation is given by  $\Delta r=\lambda/30$ .

shown in Fig. 2(a) as the  $A$  axis, and the radius of the disk is determined by  $R=a+b$ , center thickness by  $2b$ , and the shape by  $q$  with  $q=0$  corresponding to a sphere. We adopted the following shape parameters:  $q=5$ ,  $a=3.0 \mu\text{m}$ , and  $b=0.75 \mu\text{m}$  for a typical undeformed biconcave shape in our calculations. The RBC possessing these parameters has a volume of  $V=78.4 \mu\text{m}^3$ , equivalent to the volume of a sphere with a radius of  $R=2.66 \mu\text{m}$ . Two additional biconcave shapes with values of  $q=2$  and  $9$  were also used in this report to study the effect of shape variation and the isovolumetric shape changes of an RBC was realized by adjusting  $a$  and  $b$ . The corresponding parameters for these two shapes are  $q$

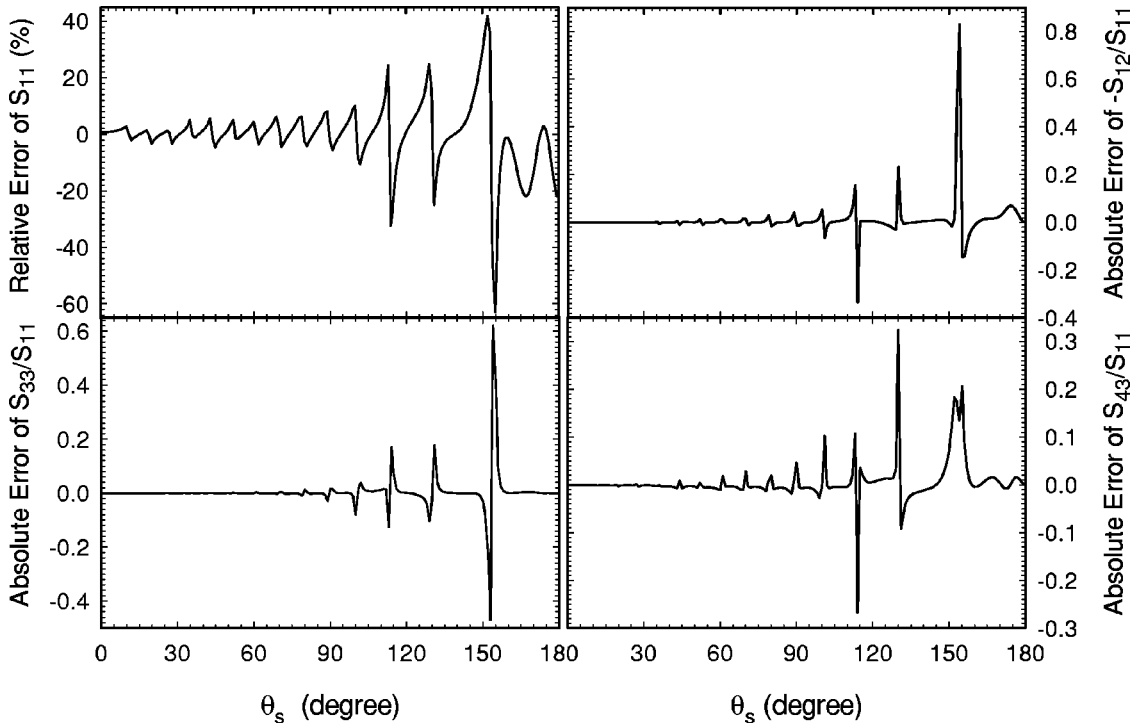


**Fig. 4** Errors in the four independent Mueller scattering matrix elements calculated by the FDTD method compared with the Mie theory for the same calculation in Fig. 3.



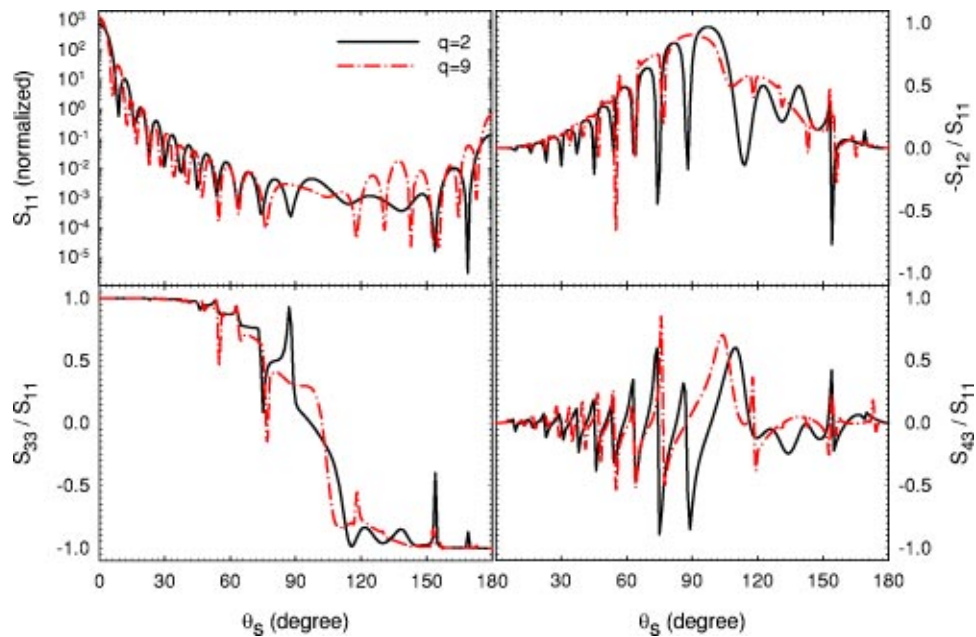


Fig. 5 Mueller scattering matrix elements as a function of scattering angle  $\theta_s$  at shape parameters of  $q=2$  and  $9$  for a biconcave RBC with  $\theta_i = 0$  deg and  $\lambda_0 = 1 \mu\text{m}$ .

$=2$ ,  $a=2.1 \mu\text{m}$ ,  $b=1.12 \mu\text{m}$ , and  $q=9$ ,  $a=3.8 \mu\text{m}$ ,  $b=0.41 \mu\text{m}$ . The cross sections of these cases are shown in Fig. 2(b). The geometrical cross section  $\sigma_g$  toward the incident light was calculated numerically for each shape and orientation in the efficiency factor calculations. This was done by projecting the illuminated portion of the RBC surface (i.e., shadowed surface region excluded) onto the plane that is perpendicular to the incident light. Although the shape function given by Eq. (4) does not fit precisely to the shape of RBC determined experimentally,<sup>37</sup> it was easy to be implemented in the code and sufficiently accurate for our purpose of investigating light scattering dependence on shape, orientation and wavelength.

### 3 Results

The scattering configuration is depicted in Fig. 2(a) with an RBC centered at the origin of the coordinate system of  $(x,y,z)$  and the incident light field propagated along the  $z$  axis. As discussed earlier, for the amplitude matrix, two incident waves with independent polarization are required. In these computations, the FDTD simulations were carried out for two incident polarization configurations with linear polarization either along the  $x$  or  $y$  axis to obtain the full amplitude matrix and subsequently the scattering matrix. The orientation of the RBC is indicated by the angle of incidence  $\theta_i$ , defined as the angle between the  $z$  axis and the  $A$  axis. The Mueller scattering matrix is, in general, a function of both scattering angle  $\theta_s$  and azimuthal angle  $\phi_s$ . In the case of normal incidence with  $\theta_i=0$  deg, the Mueller scattering matrix depends only on the scattering angle  $\theta_s$ . We chose the same grid size along the  $x$ ,  $y$ , and  $z$  directions:  $\Delta x = \Delta y = \Delta z$ .

The FDTD code was first validated by comparing with Mie theory for the case of a homogenous sphere suspended in blood plasma of refractive index  $n_p$ . The sphere was assumed

to possess the same optical properties of a normal RBC with  $n_r/n_p=1.0385$  from Ref. 8 and  $n_i=1.6804 \times 10^{-5}$  according to Fig. 1 at the wavelength of  $\lambda_0=1 \mu\text{m}$ . The radius of the sphere  $R$  was set at  $2.655 \mu\text{m}$  to obtain the same volume as an undeformed RBC. The FDTD simulation was carried out with a grid size of  $\lambda/\Delta x=30$ , where  $\lambda=\lambda_0/n_p$  is the wavelength in the blood plasma. The angular distribution of  $S_{11}$ , or the single-scattering phase function, of the Mueller scattering matrix calculated by the FDTD method is compared with that of Mie theory in Fig. 3 in a semilog scale. Errors in the FDTD calculation in comparing with Mie theory for the four nonzero independent elements of the Mueller scattering matrix are presented in Fig. 4, where the error of  $S_{11}$  is in the form of relative error and that of other elements is in the form of absolute error. The relative error of  $S_{11}$  is defined as the difference of calculated  $S_{11}$  between the two methods scaled by that of Mie theory while the absolute errors of the other elements are the differences between the results of the two methods. In general, deviations of the FDTD results from Mie theory become evident for three scattering angles large than  $90$  deg that are associated with local minima in the phase function. The largest error is observed at  $\theta_s=151$  deg; where the scattered energy is at the lowest level. The relative errors are not presented for elements other than  $S_{11}$  for these elements have values of  $0$  or close to  $0$  at some scattering angles and thus relative errors cannot be defined.

The computational resource requirements (memory and CPU time) for the 3-D FDTD problem increase with grid size according to a power law. It is observed in the current calculation that the CPU time increases approximately with the third power of grid size while the memory requirements increase approximately with a power of  $2.4$ . The choice of a suitable grid size is important to improve the code performance. To evaluate the effects of grid size, we calculated the Mueller scattering matrix of an undeformed RBC with two

**Table 1** The shape dependence ( $\theta_i=0$  deg,  $\lambda_0=1$   $\mu\text{m}$ ).

$q$	$Q_s$	$Q_a$	$g$
0	1.287	$1.09 \times 10^{-3}$	0.9913
(sphere)	(Mie: 1.311)	(Mie: $1.08 \times 10^{-3}$ )	(Mie: 0.9912)
2	0.6084	$7.20 \times 10^{-4}$	0.9916
5	0.3441	$5.27 \times 10^{-4}$	0.9930
9	0.1965	$3.90 \times 10^{-4}$	0.9904

different grid sizes of  $\lambda/\Delta x=30$  and  $\lambda/\Delta x=20$ . The results demonstrate that the effect of grid size change from  $\lambda/\Delta x=30$  to  $\lambda/\Delta x=20$  on the calculated angular distributions of light scattered by an undeformed RBC at  $\theta_i=0$  deg is negligible except near  $\theta_s=113$  deg and  $\theta_s=176$  deg, where the maximum relative errors near these two angles ( $\pm 4$  deg) were found to be 130 and 150%, respectively. However, with a grid size of  $\lambda/\Delta x=20$ , the CPU time and memory use can be reduced by a factor of 3 in comparison with  $\lambda/\Delta x=30$ . In addition, the interest of current study is on the dependence of angular distribution of light scattering on the RBC shape, orientation and light wavelength, simulations with  $\lambda/\Delta x=20$  provides sufficiently accurate results for this aspect. For these reasons, we used the grid size of  $\lambda/\Delta x=20$  for the rest of the calculations presented in this paper.

We first applied the FDTD method to investigate the effects on the angular distributions of scattered light and optical parameters caused by isovolumetric shape changes of a RBC by varying the shape parameter  $q$  in Eq. (4) from the undeformed case of  $q=5$ . The Mueller scattering matrix elements have been calculated using the FDTD method for each of the three biconcave shapes in Fig. 2(b) for a normally incident light of  $\theta_i=0$  with the same real and imaginary indices of refraction used for the sphere case at  $\lambda_0=1$   $\mu\text{m}$ . It is observed that the shape change correlates with scattering pattern change, and marked changes are evident in the phase functions  $S_{11}$  and  $S_{43}$ . As the shape deviates from the spherical shape by isovolumetrically “flattening” along the  $z$  axis, the phase function shows drastically enhanced backscattering near  $\theta_s=180$  deg by factors of more than 10, while side scattering near  $\theta_s=90$  deg demonstrates large pattern shifting. The results for  $q=2$  and 9 are plotted in Fig. 5 for the four independent elements of the Mueller scattering matrix to illustrate the pattern. The corresponding optical parameters are compared in Table 1 together with those of the sphere case of  $q=0$ , and it shows large drops in scattering and absorption power as the RBC is flattened for increasing  $q$ , but the correlation between  $g$  and  $q$  is relatively weak.

We next studied the effect of RBC's orientation on the Mueller scattering matrix elements by considering nonzero values of incident angle  $\theta_i$ . In these cases, the system loses its symmetry with respect to the  $z$  axis, and the Mueller scattering matrix elements depend on both  $\theta_s$  and  $\phi_s$ . In addition, the number of independent elements of the Mueller scattering matrix can increase to 6. For this part of the calculations, we considered only the undeformed shape of RBC with  $q=5$  at

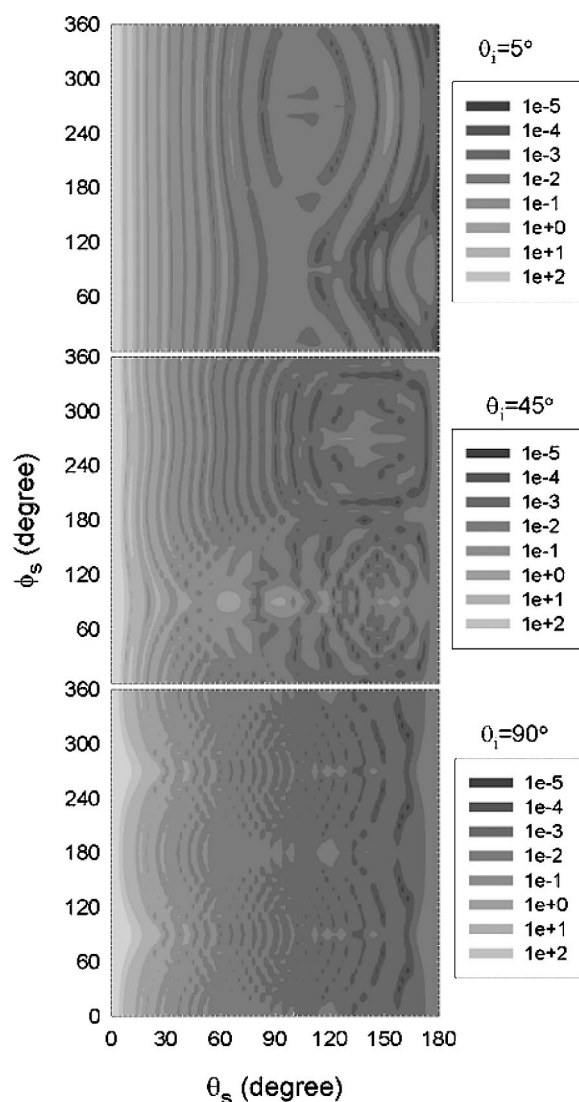


**Fig. 6** Contour plots of the phase function  $S_{11}$  as a function of  $\theta_s$  and  $\phi_s$  at different values of incident angle  $\theta_i$  for a typical RBC with  $q=5$  and  $\lambda_0=1$   $\mu\text{m}$ .

$\lambda_0=1$   $\mu\text{m}$ . The phase functions  $S_{11}(\theta_s, \phi_s)$  for different incidence angles  $\theta_i$  of 5, 45, and 90 deg are depicted in Fig. 6. Here we observe a clear dependence of the scattering pattern on  $\phi_s$  as the  $A$  axis tilted away from the  $z$  axis [see Fig. 2(a)] and a return to increased symmetry at  $\theta_i=90$  deg. Particularly, a relatively large portion of the energy is scattered near  $\phi_s=90$  deg for the case of  $\theta_i=45$  deg. The azimuthally averaged Mueller scattering matrix was obtained and four of the independent elements for different incident angles are plotted in Fig. 7 as a function of the scattering angle  $\theta_s$ . We can see that the averaging over the azimuthal angle  $\phi_s$  smooths the angular oscillations in the elements for nonzero  $\theta_i$  comparing with the case of  $\theta_i=0$  deg. The differences between the element  $S_{22}$  and  $S_{11}$  and  $S_{44}$  and  $S_{33}$  were found to be very small and thus are not presented in Fig. 7. The dependency of the optical parameters on the incident angle is plotted in Fig. 8, and it shows a clear pattern of increasing in scattering and absorption powers as the angle of incident increases, and the

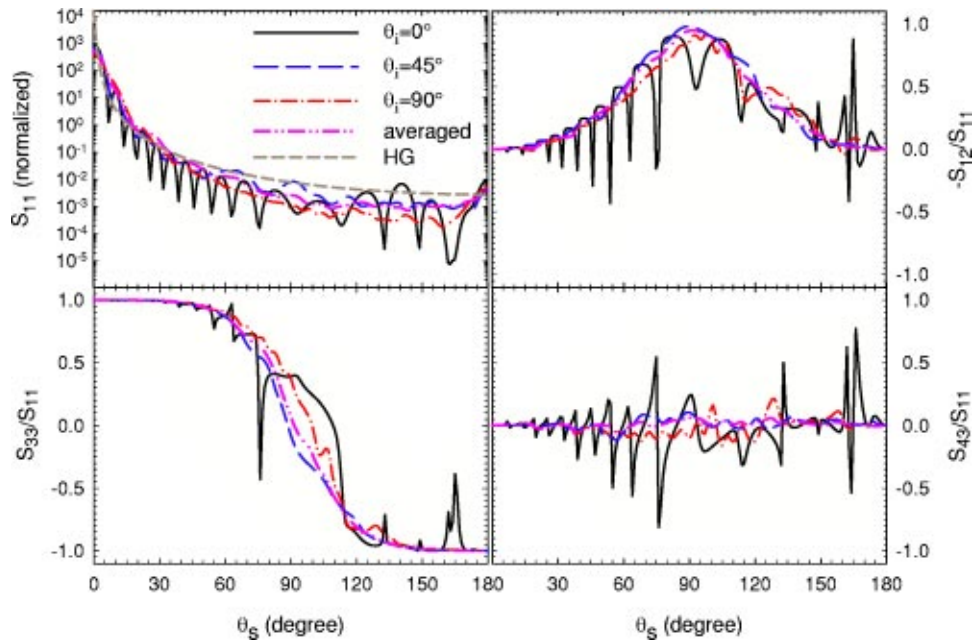


**Fig. 7** Mueller scattering matrix elements as functions of the scattering angle  $\theta_s$  for different angles of incidence  $\theta_i$  together with the corresponding elements averaged over the incident angle for a typical RBC with  $q=5$  and  $\lambda_0=1 \mu\text{m}$ . The elements were averaged over the azimuthal angle  $\phi_s$  for cases of nonzero  $\theta_i$ . The Henyey-Greenstein phase function calculated using the  $g$  averaged over the incident angle is presented with  $S_{11}$ .

decrease in  $g$  indicates that more energy is scattered into scattering angles other than the forward direction. This effect is demonstrated in the phase function by the broadened peak in the small scattering angle region for larger angles of incidence.

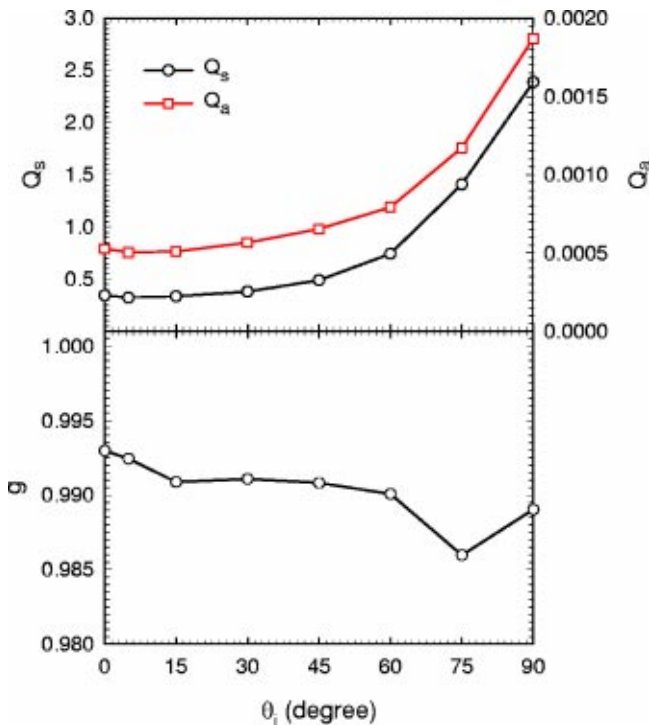


**Fig. 8** Scattering efficiency  $Q_s$ , absorption efficiency  $Q_a$ , and anisotropy factor  $g$  as functions of the incident angle  $\theta_i$  for the case defined in Fig. 7. The solid lines are meant only as guides for the eye.

For biconcave RBCs suspended in blood plasma, the orientations of the cells may be arbitrary. Experimental measurements of single scattering light distribution from a cell suspension correspond in general to calculated ones averaged over  $\phi_s$  and  $\theta_i$ . For this reason, we averaged the azimuthally averaged elements of the Mueller scattering matrix over eight incident angles between 0 and 90 deg, which resulted in smoothed curves that are also plotted in Fig. 7. The anisotropy factor corresponding to the averaged phase function is  $\bar{g} = 0.9888$ . The averaged phase function was calculated by weighting the azimuthally averaged phase function for each incident angle with its corresponding scattering cross section before normalization according to Eq. (5). The averaged efficiencies were also computed by obtaining the ratio of averaged cross sections to the averaged geometric cross section, and it yielded the average values of  $\bar{Q}_s = 0.8091$  and  $\bar{Q}_a = 8.36 \times 10^{-4}$ .

In the study of multiple light scattering in turbid tissues, a single-parameter function of Henyey-Greenstein (HG) is widely used as the phase function for single scattering:

$$P_{HG}(\cos \theta) = \frac{1}{2} \frac{1 - g^2}{(1 - 2g \cos \theta + g^2)^{3/2}} \quad (8)$$

To compare with the azimuthally averaged phase function calculated by FDTD method, the HG phase function in Eq. (8) is normalized according to Eq. (5) by dividing with a factor of  $(1/4\pi) \int_{4\pi} P_{HG}(\theta_s) d\Omega_s$ . In Fig. 7 we plotted the normalized HG phase function using the  $\bar{g}$  obtained earlier compare with the averaged  $S_{11}$  from our FDTD calculation. It is evident that the two phase functions differ significantly near the forward direction and between 60 and 170 deg of scattering angle.

We also examined the scattering properties of an undeformed RBC with  $q=5$  at different values of wavelength  $\lambda_0$ .



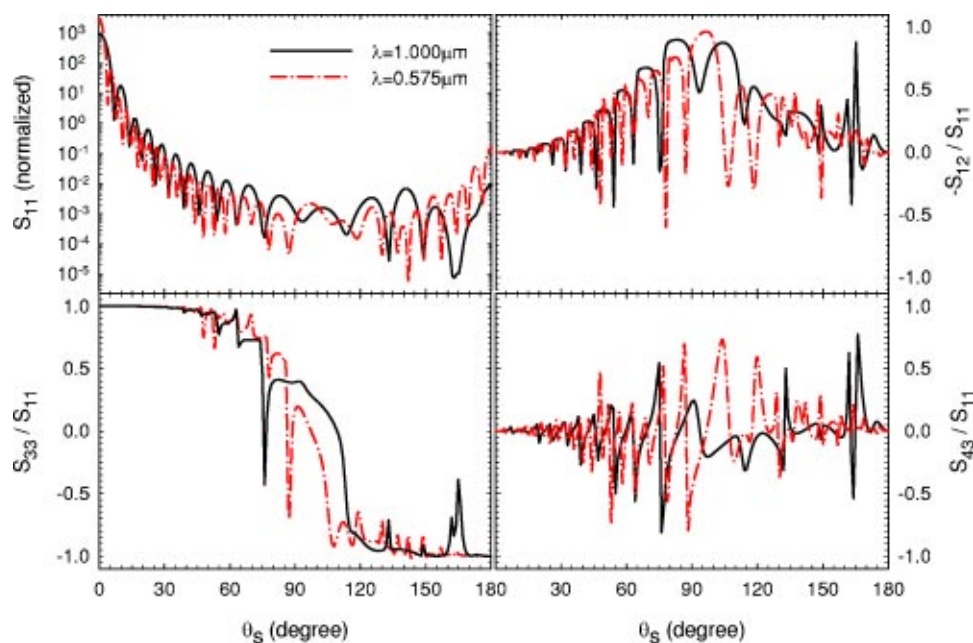


**Fig. 9** Comparisons of the angular distribution of the Mueller scattering matrix elements at wavelengths  $\lambda_0=0.575 \mu\text{m}$  and  $1 \mu\text{m}$  for the case of  $\theta_i=0 \text{ deg}$  and  $q=5$ .

It is well known that scattering and absorption cross sections are closely related to the complex index of refraction and that the frequency of oscillation in the phase function depends on the size parameter  $\alpha$ . To study the effect of the wavelength on light scattering by an RBC, we chose two additional wavelengths corresponding to a maximum and a minimum in the imaginary index  $n_i$  between 400 and 1000 nm (see Fig. 1):  $\lambda_0=0.575 \mu\text{m}$  with  $n_i=5.4 \times 10^{-4}$  and  $\lambda_0=0.700 \mu\text{m}$  with  $n_i=4.3 \times 10^{-6}$ . The real indices are taken to be  $n_r/n_p=1.0386$  and  $1.0385$ , respectively, according to Ref. 8. The Mueller scattering matrix elements for a typically shaped RBC of  $q=5$  with a normal incidence of  $\theta_i=0 \text{ deg}$  at these two wavelengths are calculated and the results for  $\lambda_0=0.575 \mu\text{m}$  is compared in Fig. 9 with the case of  $\lambda_0=1 \mu\text{m}$  to show the general trend while the optical parameters are listed in Table 2 together with those of  $\lambda_0=1 \mu\text{m}$ . It is well known from Mie theory that in the case spheres, an increasing size parameter  $\alpha$  leads to more oscillation in the angular distribution of phase function. This trend is confirmed by the results in Fig. 9 and those of the  $\lambda_0=0.7 \mu\text{m}$  case. These results also demonstrate a previously known pattern that at shorter wavelengths (i.e., large size parameter), the RBC scatters more light near the forward direction and thus decreases the scattering at large angles, causing a larger  $g$ .

**Table 2** The wavelength dependence ( $q=5$ ,  $\theta_i=0 \text{ deg}$ ).

$\lambda_0$	$n_i$	$Q_s$	$Q_a$	$g$
$0.575 \mu\text{m}$	$5.4 \times 10^{-4}$	0.9319	$2.83 \times 10^{-2}$	0.9964
$0.700 \mu\text{m}$	$4.3 \times 10^{-6}$	0.6485	$1.87 \times 10^{-4}$	0.9952
$1.000 \mu\text{m}$	$1.68 \times 10^{-5}$	0.3441	$5.27 \times 10^{-4}$	0.9930

The optical parameters listed in Table 2 show that the scattering efficiency of an RBC increases with decreasing wavelength, and the absorption efficiency of an RBC relates positively with the imaginary part of the index ( $n_i$ ) with the smallest value at  $\lambda=0.700 \mu\text{m}$  and the largest at  $\lambda=0.575 \mu\text{m}$ .

#### 4 Discussion

In this paper, we validated a serial FDTD code for accurate modeling of light scattering by a biconcave RBC and obtained the Mueller scattering matrix elements as a function of scattering angles. Our results reveal a direction correlation between angular distribution of Mueller scattering matrix elements and the shape and orientation of a biconcave RBC at different light wavelengths. It was shown that the scattering and absorption efficiencies decrease as the RBC is flattened, and those parameters increase as the incident light tilts from the axis of symmetry of the cell. Results obtained at different wavelengths indicate that the scattering efficiency increases rapidly with decreasing wavelength, while the absorption efficiency depends sensitively on the imaginary part of the refractive index of the cell.

As presented in Figs. 3 and 4 for the case of a sphere, the errors in the Mueller scattering matrix calculations in our FDTD method are significant only at a few isolated scattering angles where the scattered fields are very weak, and the deviation of FDTD results from the Mie theory is often dominated by errors near the backscattering direction of  $\theta_s=180 \text{ deg}$ . Although similar errors are also observed in other calculations,<sup>17,21</sup> it appears more pronounced in the large scattering angle region for scatterers like biological cells in a fluid, particularly near the backscattering direction. This may be attributed to the fact that the relative index of refraction in the case of light scattering from biological cells in a fluid is



very close to 1. In this case, the phase function is featured with a strong peak in the forward direction, which drops rapidly with increasing scattering angle and a dynamic range of more than seven orders of magnitude. This feature of the phase function subjects the low-scattering-energy region, namely, the large scattering region, to higher relative errors. The sources of errors in this calculation may come from the use of large grid size  $\Delta x$ , shorted time marching duration  $\Delta T$ , and deficiency in the absorbing boundary condition. Large  $\Delta x$  causes imperfect fitting of the spherical surface with the finite sized grid used in the calculations, while small  $\Delta T$  leaves some measurable scattered energy uncoun-<sup>17</sup> Reducing either grid size or increasing time-marching duration can increase the accuracy of FDTD simulations at the expense of higher computational cost. The PML absorption boundary condition used in this calculation is very efficient for most calculations, but for the reason discussed earlier, it seems not sufficient for the large dynamic range of the phase function in this case. A recently introduced uniaxial perfectly matched layer (UPML) absorption boundary condition<sup>16,38</sup> reportedly may provide improved efficiency for certain cases. We are currently testing this possibility by implementing UPML into our program.

Since a mature human RBC contains no internal structure, the angular distribution of  $S_{34}$  does not display systematic patterns of changes for different shapes, orientations, and wavelengths, as observed in some cases where internal structure was presented.<sup>29,33</sup> On the other hand, it is interesting to notice that the phase function  $S_{11}$  in Fig. 5 exhibits a very strong enhancement near  $\theta_s = 180$  deg when the shape of the biconcave RBC deviates from the typical undeformed shape of  $q = 5$ . As discussed earlier, the use of a relatively large grid size of  $\lambda/\Delta x = 20$  may contribute up to 150% simulation errors in this region, or a factor of 1.5, the changes in the back-scattering probabilities, however, are much larger than that when  $q$  changes either to 2 or 9. If the  $S_{11}$  is integrated from  $\theta_s = 170$  to 180 deg to obtain  $(S_{11})_b$ , we found that  $(S_{11})_b$  of an RBC increases from 0.0712 for the case of  $q = 5$  to 1.14 for  $q = 2$  and 4.35 for  $q = 9$ . Furthermore, one can observe from Fig. 7 that the  $S_{11}$  for the case of  $q = 5$  changes very little near  $\theta_s = 180$  deg for different angle of incidence  $\theta_i$ . These results in combination suggest that enhanced back-scattering from RBCs of biconcave shapes may be used as a sensitive tool to measure changes in RBC shape.

### Acknowledgments

This work was supported in part by National Institutes of Health (NIH) Grant No. 1R15GM70798-01 and the calculations were made possible in part by National Partnership for Advanced Computational Infrastructure (NPACI) and North Carolina Supercomputer Center (NCSC) through supercomputer time allocations. JQL is grateful to Ms. Ruth Marinshaw and Dr. Shubin Liu at Academic Technology and Networks (ATN) at the University of North Carolina, Chapel Hill, for the assistance of some of the larger calculations.

### References

1. J. W. M. Visser, "Analysis and sorting of blood and bone marrow cells," Chap. 33 in *Flow Cytometry and Sorting*, M. R. Melamed, T. Lindmo, and M. L. Mendelsohn, Eds., 2nd ed., Wiley, New York (1990).
2. W. Groner, N. Mohandas, and M. Bessis, "New optical technique for measuring erythrocyte deformability with the ektacytometer," *Clin. Chem.* **26**, 1435–1442 (1980).
3. P. Mazoner, S. Muller, and H. El Azouzi, "On intensity reinforcements in small-angle light scattering patterns of erythrocytes under shear," *Eur. Biophys. J.* **26**, 247–252 (1997).
4. M. Rasia and A. Bollini, "Red blood cell shape as a function of medium's ionic strength and pH," *Biochim. Biophys. Acta* **1372**, 198–204 (1998).
5. G. D. Pederson, N. J. McCormick, and L. O. Reynolds, "Transport calculations for light scattering in blood," *Biophys. J.* **16**, 199–207 (1976).
6. D. H. Tycko, M. H. Metz, E. A. Epstein, and A. Grinbaum, "Flow-cytometric light scattering measurement of red blood cell volume and hemoglobin concentration," *Appl. Opt.* **24**, 1355–1365 (1985).
7. G. J. Streekstra, A. G. Hoekstra, and R. M. Heethaar, "Anomalous diffraction by arbitrarily oriented ellipsoids: applications in ektacytometry," *Appl. Opt.* **33**, 7288–7296 (1994).
8. A. G. Borovoi, E. I. Naats, and U. G. Oppel, "Scattering of light by a red blood cell," *J. Biomed. Opt.* **3**, 364–372 (1998).
9. S. V. Tsinopoulos and D. Polyzos, "Scattering of He Ne laser light by an average-sized red blood cell," *Appl. Opt.* **38**, 5499–5510 (1999).
10. S. V. Tsinopoulos, E. J. Sellountos, and D. Polyzos, "Light scattering by aggregated red blood cells," *Appl. Opt.* **41**, 1408–1417 (2002).
11. L. T. Perelman, V. Backman, M. Wallace, G. Zonios, R. Manoharan, A. Nusrat, S. Shields, M. Seiler, C. Lima, T. Hamano, I. Itzkan, J. Van Dam, J. M. Crawford, and M. S. Feld, "Observation of periodic fine structure in reflectance from biological tissue: a new technique for measuring nuclear size distribution," *Phys. Rev. Lett.* **80**, 627–630 (1998).
12. M. I. Mishchenko, J. W. Hovenier, and L. D. Travis, Eds., *Light Scattering by Nonspherical Particles*, Academic Press, San Diego, CA (2000).
13. M. I. Mishchenko, "Light scattering by randomly oriented axially symmetric particles," *J. Opt. Soc. Am. A* **8**, 871–882 (1991).
14. B. T. Draine, "The discrete-dipole approximation and its application to interstellar graphite grains," *Astrophys. J.* **333**, 848–872 (1988).
15. B. T. Draine and P. J. Flatau, "Discrete-dipole approximation for light calculations," *J. Opt. Soc. Am. A* **11**, 1491–1499 (1994).
16. A. Taflov and S. C. Hagness, *Computational Electrodynamics: The Finite-Difference Time-Domain Method*, 2nd ed., Artech House, Boston (2000).
17. P. Yang and K. N. Liou, "Finite-difference time domain method for light scattering by small ice crystals in three-dimensional space," *J. Opt. Soc. Am. A* **13**, 2072–2085 (1996).
18. P. Yang, K. N. Liou, M. I. Mishchenko, and B. C. Gao, "An efficient finite-difference time domain scheme for light scattering by dielectric particles: application to aerosols," *Appl. Opt.* **39**, 3727–3737 (2000).
19. W. B. Sun, N. G. Leob, and Q. Fu, "Finite-difference time-domain solution of light scattering and absorption by particles in an absorbing medium," *Appl. Opt.* **41**, 5728–5743 (2002).
20. W. B. Sun, Q. Fu, and Z. Chen, "Finite-difference time-domain solution of light scattering by dielectric particles with perfectly matched layer absorbing boundary conditions," *Appl. Opt.* **38**, 3141–3151 (1999).
21. A. Dunn and R. Richard-Kortum, "Three-dimensional computation of light scattering from cells," *IEEE J. Sel. Top. Quantum Electron.* **2**, 898–890 (1996).
22. D. Arifler, M. Guillaud, A. Carraro, A. Malpica, M. Follen, and R. Richards-Kortum, "Light scattering from normal and dysplastic cervical cells at different epithelial depths: finite-difference time-domain modeling with a perfectly matched layer boundary condition," *J. Biomed. Opt.* **8**, 484–494 (2003).
23. J. Q. Lu, P. Yang, and X.-H. Hu, "Accurate simulation of light scattering by a red blood cell using the FDTD method," in *Conf. on Lasers and Electro-Optics Technical Digest 553–554, CLEO 2002*, (2002).
24. J. Q. Lu and X. H. Hu, "Modeling of light scattering and distribution in biological systems," 541–563 in *Recent Research Developments in Optics*, Vol. 2, *Research Signpost*, (Trivandrum, India, 2002) Part II.
25. P. Yang and K. N. Liou, "Finite difference time domain method for light scattering by nonspherical and inhomogeneous particles," Chap. 7 in *Light Scattering by Nonspherical Particles*, M. I. Mishchenko, J. W. Hovenier, and L. D. Travis, Eds., Academic Press, San Diego, CA (1999).
26. J. D. Jackson, *Classical Electrodynamics*, 3rd ed., Wiley, New York (1999).

27. C. F. Bohren and D. R. Huffman, *Absorption and Scattering of Light by Small Particles*, Wiley, New York (1987).
28. J. P. Berenger, "Three-dimensional perfectly matched layer for the absorption of electromagnetic waves," *J. Comput. Phys.* **127**, 363–379 (1996).
29. W. S. Bickel and M. E. Stafford, "Polarized light scattering from biological systems: a technique for cell differentiation," *J. Biol. Phys.* **9**, 53–66 (1981).
30. V. Backman, R. Gurjar, K. Badizadegan, R. Dasari, I. Itzkan, L. T. Perelman, and M. S. Feld, "Polarized light scattering spectroscopy for quantitative measurement of epithelial cellular structures *in situ*," *IEEE J. Sel. Top. Quantum Electron.* **5**, 1019–1026 (1999).
31. J. R. Mourant, T. M. Johnson, S. Carpenter, A. Guerra, T. Aida, and J. P. Freyer, "Polarized angular dependent spectroscopy of epithelial cells and epithelial cell nuclei to determine the size scale of scattering structures," *J. Biomed. Opt.* **7**, 378–387 (2002).
32. H. C. van de Hulst, *Light Scattering by Small Particles*, Wiley, New York (1957).
33. G. C. Salzman, S. B. Singham, R. G. Johnston, and C. F. Bohren, "Light scattering and cytometry," Chap. 5 in *Flow Cytometry and Sorting*, M. R. Melamed, T. Lindmo, and M. L. Mendelsohn, Eds., 2nd ed., Wiley, New York (1990).
34. O. W. Van Assendelft, *Spectrophotometry of Haemoglobin Derivatives*, C. C. Thomas, Springfield, IL (1970).
35. R. B. Pennell, "Composition of normal human red cells," in *The Red Blood Cell*, C. Bishop and D. M. Surgenors, Eds., Academic Press, New York (1964).
36. G. Cicco and A. Pirrelli, "Red blood cell (RBC) deformability, RBC aggregability and tissue oxygenation in hypertension," *Clin. Hemorheol Microcirc* **21**, 169–177 (1999).
37. Y. C. Fung, W. C. O. Tsang, and P. Patitucci, "High-resolution data on the geometry of red blood cells," *Biorheology* **18**, 369–385 (1981).
38. S. D. Gedney, "An anisotropic perfectly matched layer absorbing media for the truncation of FDTD lattices," *IEEE Trans. Antennas Propag.* **44**, 1630–1639 (1996).